

VAPO: Visibility-Aware Keypoint Localization for Efficient 6DoF Object Pose Estimation

Ruyi Lian, Yuewei Lin, Longin Jan Latecki, Haibin Ling *Fellow, IEEE*

Abstract—Localizing predefined 3D keypoints in a 2D image is an effective way to establish 3D-2D correspondences for 6DoF object pose estimation. However, unreliable localization results of invisible keypoints degrade the quality of correspondences. In this paper, we address this issue by localizing the important keypoints in terms of visibility. Since keypoint visibility information is currently missing in the dataset collection process, we propose an efficient way to generate binary visibility labels from available object-level annotations, for keypoints of both asymmetric objects and symmetric objects. We further derive real-valued visibility-aware importance from binary labels based on the PageRank algorithm. Taking advantage of the flexibility of our visibility-aware importance, we construct VAPO (Visibility-Aware POse estimator) by integrating the visibility-aware importance with a state-of-the-art pose estimation algorithm, along with additional positional encoding. VAPO can work in both CAD-based and CAD-free settings. Extensive experiments are conducted on popular pose estimation benchmarks including Linemod, Linemod-Occlusion, and YCB-V. The results show that, VAPO significantly improves both the keypoint correspondences and final estimated poses, and clearly achieves state-of-the-art performances.

Index Terms—6DoF pose estimation, Keypoint localization, Visibility.

I. INTRODUCTION

GIVEN a single input RGB image, the instance-level 6DoF object pose estimator recovers rotation and translation of a rigid object with respect to a calibrated camera. The estimated pose information is crucial in numerous real-world applications, including robot manipulation [1]–[3], autonomous driving [4]–[6], augmented reality [7], [8], 3D reconstruction [9], [10], *etc.* To increase the robustness under various imaging conditions, most existing methods [11]–[21] first generate correspondences between 2D image pixels and 3D object points, and then regress the pose via any available Perspective-n-Point (PnP) solver [22]–[24].

Based on the correspondence estimation process, previous methods can be divided into two categories. The first kind of methods [16]–[18], [20], [23], [25] estimate corresponding 3D coordinate on the object surface for each 2D pixel, which can be treated as an image-to-image translation task. The second kind of methods [11], [12], [15], [21], [26] localize

predefined 3D keypoints in the input image to obtain 3D-2D correspondences. Compared with image-to-image translation based methods, keypoint-based methods more efficiently encode the object geometry information, which facilitates the pose estimation process. The pioneering keypoint-based works localize the eight corners of the 3D object bounding box [11], [12]. The follow-up works [15], [26] adopt sparse keypoints (*e.g.*, 8 keypoints) sampled from the object surface. Recently, CheckerPose [21] is proposed to generate dense correspondences via localizing dense 3D keypoints and it achieves state-of-the-art performance for object pose estimation.

To obtain better correspondences for object pose estimation, a great amount of effort has been devoted to improve the localization precision of each keypoint. However, existing keypoint-based methods share a common limitation, *i.e.*, a large portion of predefined keypoints are invisible due to occlusion or self-occlusion. Without direct observations, localizing such keypoints often leads to unreliable results. Since the ultimate goal of keypoint localization is to establish reliable 3D-2D correspondences for 6DoF pose estimation, it may not be necessary to localize each predefined keypoint.

To overcome this issue, we propose to estimate visibility-aware importance for each keypoint, and discard unimportant keypoints before localization. As a starting point, keypoint visibility can be represented as a binary value. We notice that such information is already manually annotated in datasets from other domains, *e.g.*, human pose estimation [27], [28]. However, annotations of keypoint visibility are currently missing in 6DoF object pose datasets. To avoid the expensive manual annotation process, we propose an efficient way to generate visibility labels from available object-level annotations. Visibility is decomposed into two binary terms w.r.t. external occlusion and internal self-occlusion. The external visibility term can be obtained from object segmentation masks. The internal visibility term can be determined based on surface normals and camera ray directions, inspired by back-face culling [29], [30] in rendering. For symmetric objects, we derive modified computation to ensure consistency.

Besides binary labels, we further derive real-valued measure to comprehensively reflect the visibility-aware importance of each keypoint. To do this, we create a k -nearest neighbor (k -NN) graph from the predefined keypoints, and measure the closeness of each keypoint to visible ones as importance. We utilize Personalized PageRank (PPR) [31] as our proximity measure, and derive an analytical formula of importance which can be efficiently evaluated.

Ruyi Lian and Haibin Ling are with the Department of Computer Science, Stony Brook University, New York, NY 11794 USA (e-mail: rliian@cs.stonybrook.edu; hling@cs.stonybrook.edu).

Yuewei Lin is with the Computational Science Initiative, Brookhaven National Laboratory, Upton, NY 11973 USA (e-mail: ywlin@bnl.gov).

Longin Jan Latecki is with the Department of Computer and Information Sciences, Temple University, Philadelphia, PA 19122 USA (e-mail: latecki@temple.edu).

Our visibility-aware importance can be seamlessly integrated into existing keypoint-based 6DoF pose estimator to boost performance. We add a visibility-aware importance predictor before keypoint localization to eliminate keypoints with low importance. To enhance the embeddings of the selected keypoints, we use positional encoding and adopt a two-stage training strategy to efficiently train our pose estimator. Furthermore, our method can easily adapt to a more general setting where precise 3D CAD model is unavailable.

To summarize, we make the following contributions:

- We propose to localize important keypoints in terms of visibility, to obtain high-quality 3D-2D correspondences for 6DoF object pose estimation.
- From object-level annotations, we derive an efficient way to generate binary keypoint visibility labels, for both asymmetric objects and symmetric ones.
- We further derive a concise analytic formula to produce real-valued visibility-aware keypoint importance based on Personalized PageRank.
- We demonstrate that our visibility-aware importance can be easily incorporated to existing keypoint-based method and work for both CAD-based and CAD-free settings.

We conduct extensive experiments on Linemod [32], Linemod-Occlusion [33], and YCB-V [34] to demonstrate the effectiveness of our method.

II. RELATED WORK

In this section, we review previous studies related to our work, including 6DoF pose estimation from RGB inputs and applications of visibility estimation.

Direct Methods. Traditionally, object poses are estimated by template matching with hand-crafted features [35]–[37], which can not work well on textureless objects. Features learned from neural networks are also investigated to directly produce the final estimated poses [34], [38]–[41]. However, due to the nonlinearity of 3D rotations, direct methods are still unstable without predicting intermediate geometric representations, *e.g.*, 3D-2D correspondences.

Image-to-image Translation Based Methods. One popular way to establish 3D-2D correspondences can be regarded as an image-to-image translation task [17]. Specifically, for each 2D pixel, the corresponding 3D point on the object surface is predicted in the object frame [17], [18], [23], [25]. The 3D coordinates can also be represented as UV-maps [16], local surface embeddings [42], hierarchical binary encodings [20], *etc.* The dense correspondences are robust against various imaging conditions, such as occlusions, background clutter, *etc.* With the correspondences, object pose can be recovered via existing PnP solvers [22], [24], coupled with RANSAC to remove outliers. Recent methods [23], [25], [43] also use neural networks to produce final poses from the correspondences.

Keypoint-based Methods. Localizing predefined keypoints in the input image is also widely used for constructing 3D-2D correspondences. For simplicity, previous works [11]–[14], [44], [45] localize the 3D object bounding box corners. Other works [15], [21], [26] also adopt keypoints on the object surface obtained via farthest point sampling (FPS),

which tend to achieve better performance since they are closely related to the object pixels. While existing methods mainly utilize sparse keypoints (*e.g.*, 8 keypoints), the recently proposed CheckerPose [21] localizes dense keypoints (*e.g.*, 512 keypoints) to construct dense 3D-2D correspondences, increasing the robustness similar to the image-to-image translation based methods. Though previous methods demonstrate the importance of predefining proper keypoints, few of them deals directly with the fact that no keypoint can always be visible in any input image.

CAD-Free Object Pose Estimation. The methods discussed above require high-fidelity 3D CAD models which may not be available in real-world applications. To remove the dependence on precise CAD models, CAD-free object pose estimation methods have been studied recently. RLLG [46] learns 2D-3D correspondences via multi-view geometric constraints. OnePose [47] builds a sparse SfM model from video scan of the object in interest, and obtains 3D-2D correspondences between the query image and SfM model via a keypoint-based matching network. OnePose++ [48] instead utilizes a keypoint-free feature matching pipeline to improve the performance on low-textured objects. GS-Pose [49] adopts 3D Gaussian Splatting [50] to build explicit representation of the object of interest.

Visibility Estimation for 3D Vision and Graphs. For an object in the 3D space, not all parts are visible in its 2D images. For rigid pose estimation, visibility can be used to select reliable correspondences [21], [51]. Still, each correspondence is generated despite its visibility. Differentiable surface visibility is developed to facilitate render-and-compare framework [52]. Visibility can also be efficiently estimated in online tracking with a known initial pose and smooth changes [53]. For nonrigid pose estimation, keypoint localization results are usually represented as heatmaps, and visibility can be implicitly interpreted from heatmaps [54]–[56]. Moreover, keypoint visibility is manually annotated in various datasets [27], [28], [57], and can be used as supervision signals [58], [59]. Beyond pose estimation, visibility determination also facilitates various tasks in computer vision and graphics. In rendering of large polygonal models, back-facing polygons are eliminated to speed up the rendering process [29], [30]. Visibility can also be utilized for mesh simplification [60], point cloud visualization [61], [62], novel view generation [63]–[67], multi-view aggregation [68], [69], *etc.*

Our work follows the keypoint-based framework for 6DoF pose estimation. We focus on keypoints with high visibility-aware importance, and effectively generate supervision signals from object-level annotations. Our method can be applied to both CAD-based setting and CAD-free setting.

III. METHOD

Our work focuses on instance-level pose estimation for a rigid object O . In the classical setting where the CAD model of O is available, we sample 3D keypoints \mathcal{P} over the object surface, and estimate the importance of each keypoint $\mathbf{p} \in \mathcal{P}$ w.r.t. visibility in the input RGB image I . We then localize the

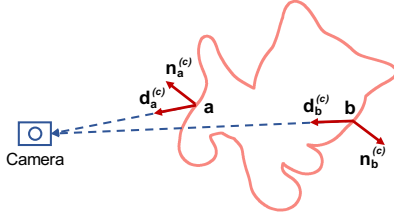


Fig. 1. **Illustration of keypoint internal visibility.** Inspired by back-face culling [29], [30] in rendering, we compute the internal visibility based on the inner product between the directional vector towards the camera (e.g., $\mathbf{d}_a^{(c)}$) and the normal vector (e.g., $\mathbf{n}_a^{(c)}$).

subset of \mathcal{P} with high importance, and obtain rotation $\mathbf{R} \in SO(3)$ and translation $\mathbf{t} \in \mathbb{R}^3$ from the localization results via a PnP solver [22], [24]. Furthermore, our method can be easily extend to the CAD-free setting. We describe our method, named VAPO (Visibility-Aware POse estimator), in details as follows.

A. Generating Visibility Labels from Object-Level Annotations

Keypoint-level annotations are typically unavailable in existing 6DoF object pose datasets, such as Linemod [32], Linemod-Occlusion [33], YCB-V [34], *etc.* While keypoint visibility labels are provided by datasets from other domains, e.g., Leeds Sports Poses [27], MPII Human Pose [28], COCO [57], *etc.*, such labels require expensive human labelling efforts. Moreover, there is no canonical way to predefine keypoints for 6DoF pose. Even though one can manually annotate the visibility of a specific set of keypoints, missing label issue still arises when an object pose estimator utilizes a different set of keypoints, e.g., denser keypoints.

To avoid expensive manual annotation and provide flexibility for different 3D keypoints \mathcal{P} , we instead seek an efficient way to generate visibility labels from available object-level annotation, *i.e.*, rotation \mathbf{R} , translation \mathbf{t} , and object segmentation masks M . A keypoint $\mathbf{p} \in \mathcal{P}$ is visible if and only if it is free from both occlusions and self-occlusions. Thus we can decompose visibility into two binary terms: the external visibility $V_{\text{ex}}(\mathbf{p}) \in \{0, 1\}$ w.r.t. occlusions from other objects, and the internal visibility $V_{\text{in}}(\mathbf{p}) \in \{0, 1\}$ w.r.t. self-occlusions. The overall visibility $V(\mathbf{p}) \in \{0, 1\}$ can be computed by

$$V(\mathbf{p}) = V_{\text{ex}}(\mathbf{p}) \times V_{\text{in}}(\mathbf{p}), \quad (1)$$

and keypoint \mathbf{p} satisfies $V(\mathbf{p}) = 1$ if and only if $V_{\text{ex}}(\mathbf{p}) = 1$ and $V_{\text{in}}(\mathbf{p}) = 1$.

Since the visible segmentation mask M_{vis} of the object O reflects occlusions from other objects, we can determine $V_{\text{ex}}(\mathbf{p})$ by

$$V_{\text{ex}}(\mathbf{p}) = \begin{cases} 1, & \text{if } \pi(\mathbf{p}; \mathbf{R}, \mathbf{t}) \in M_{\text{vis}} \\ 0, & \text{otherwise} \end{cases}, \quad (2)$$

where $\pi(\mathbf{p}; \mathbf{R}, \mathbf{t})$ is the perspective projection of \mathbf{p} using pose (\mathbf{R}, \mathbf{t}) .

To determine whether keypoint $\mathbf{p} \in \mathcal{P}$ is self-occluded, we can check whether the direction from \mathbf{p} towards the camera

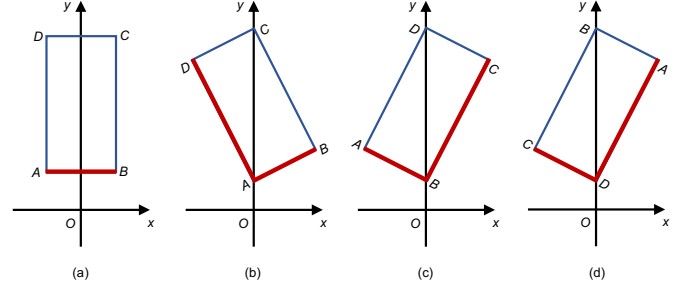


Fig. 2. **2D Illustration of how annotated poses affect keypoint visibility labels for a symmetric object.** In the camera space, the camera is placed at the origin O and looks at the direction $y > 0$. The visible points are highlighted in red. (a) The object is translated along y -axis by \mathbf{t} . (b) The object is slightly rotated counterclockwise around its center and then translated by \mathbf{t} . (c) The object is slightly rotated clockwise and then translated by \mathbf{t} , but the visible points are significantly different from (b). (d) The object is rotated by a larger degree to get equivalent appearance of (c), while the visible points highly overlap with (b).

has additional intersections with the object surface. However, it is time-consuming to check the intersections on the fly during training. Inspired by back-face culling [29], [30] in rendering, we compute $V_{\text{in}}(\mathbf{p})$ by

$$V_{\text{in}}(\mathbf{p}) = \begin{cases} 1, & \text{if } \mathbf{d}_p^{(c)} \cdot \mathbf{n}_p^{(c)} > 0 \\ 0, & \text{otherwise} \end{cases}, \quad (3)$$

where $\mathbf{d}_p^{(c)}$ denotes the direction from \mathbf{p} towards the camera in the camera space, $\mathbf{n}_p^{(c)}$ denotes the surface normal at \mathbf{p} in the camera space, and “ \cdot ” indicates the dot product. As illustrated in Figure 1, keypoint \mathbf{a} is internally visible while \mathbf{b} is internally invisible according to Eq. (3). In the camera space, the camera is placed at the origin $[0, 0, 0]^T$, and then

$$\mathbf{d}_p^{(c)} = -\mathbf{p}^{(c)} = -(\mathbf{R}\mathbf{p} + \mathbf{t}), \quad (4)$$

where $\mathbf{p}^{(c)}$ is the keypoint coordinate in the camera space. When the 3D CAD model is available, we have access to the surface normal \mathbf{n}_p in the object frame, and we get

$$\mathbf{n}_p^{(c)} = \mathbf{R}\mathbf{n}_p, \quad (5)$$

thus Eq. (3) can be efficiently computed from available object-level annotations.

For a convex object, $V_{\text{in}}(\mathbf{p}) = 1$ is a necessary and sufficient condition for \mathbf{p} being not self-occluded. For a non-convex object, $V_{\text{in}}(\mathbf{p}) = 1$ is a necessary condition, and we use Eq. (3) for several reasons. Firstly, if $V_{\text{in}}(\mathbf{p}) = 0$, then \mathbf{p} must be self-occluded, and we can safely eliminate \mathbf{p} or reduce the importance of \mathbf{p} in localization process. Secondly, a non-convex object tends to have a complex shape, and we might obtain better understanding of the object by keeping a small portion of self-occluded keypoints. Thirdly, Eq. (3) is easy to compute based on available object-level annotations, which significantly facilitates the training process.

B. Handling Visibility of Symmetric Objects

For a symmetric object, an input image corresponds to multiple equivalent poses w.r.t. the symmetry transformations S . In practice, only one of the equivalent poses is annotated in

dataset generation process. For different images with similar appearances, the annotated poses may be dramatically different.

From the perspective of keypoint visibility, it is not optimal to directly use the annotated poses to generate visibility labels. Let us consider a 2D case without external occlusion for simplicity. As illustrated in Figure 2 (a), the symmetry transformations \mathcal{S} contain the identity matrix \mathbf{I} and the one that rotates the object around the center by 180° . The object is annotated with different poses in Figure 2 (c) and (d). Since the poses are equivalent w.r.t. \mathcal{S} , the appearances look identical. However, the visibility label for each keypoint is completely different. The inconsistency of keypoint visibility labels is problematic for training a robust visibility classifier.

To enforce the consistency of keypoint visibility labels, we can transform the original annotated pose (\mathbf{R}, \mathbf{t}) to a canonical one with a proper symmetry transformation $\tilde{\mathbf{S}} \in \mathcal{S}$. A naive way to select $\tilde{\mathbf{S}}$ is to minimize the distance between the transformed rotation and the identity matrix \mathbf{I} . However, this strategy may still cause inconsistency of keypoint visibility labels. As shown in Figure 2 (b), the annotated pose is a combination of a slight counterclockwise rotation around object center (denoted as \mathbf{R}_1) and a translation \mathbf{t} along y -axis, and the corresponding visible points are on the edges AB and DA . While in Figure 2 (c), the annotated rotation is a slight clockwise rotation around center (denoted as \mathbf{R}_2), and the corresponding visible points appear on the edges AB and BC . Since $|BC| = |DA| \gg |AB|$, the visible points corresponding to $(\mathbf{R}_1, \mathbf{t})$ and $(\mathbf{R}_2, \mathbf{t})$ are dramatically different, even though \mathbf{R}_1 and \mathbf{R}_2 are both close to the identity matrix \mathbf{I} . As shown in Figure 2 (d), the object is rotated by a larger degree. The visible points appear on the edges DA and CD , which highly overlap with the visible points of (b).

Therefore, we modify the annotated pose to maximize the number of internally visible keypoints in a fixed subset of keypoints \mathcal{P}_{sym} . We consider internal visibility V_{in} because self-occlusion always exists and is not effected by external objects.

For an object with discrete symmetry, before the whole training process, we obtain \mathcal{P}_{sym} by finding the largest visible subset under sampled poses. In practice, we uniformly sample 2,562 rotation matrices in $SO(3)$, and use a fixed translation \mathbf{t} along the camera looking direction. Then during training, we can enumerate the finite equivalent poses to find the one maximizing internally visible keypoints in \mathcal{P}_{sym} . In practice, we usually just need to compare 2 equivalent poses, so the additional computational cost is negligible.

For an object with continuous symmetry, a straightforward way is to discretize the symmetry transformations to get finite transformations, then find the desired equivalent pose just like discrete symmetry. Though this solution is feasible, it needs to enumerate a lot of equivalent poses to ensure the accuracy. We instead derive analytic formulas that are easy to evaluate. With Eq. (4) and Eq. (5), we get

$$\begin{aligned} -\mathbf{d}_p^{(c)} \cdot \mathbf{n}_p^{(c)} &= (\mathbf{R}\mathbf{p} + \mathbf{t})^\top (\mathbf{R}\mathbf{n}_p) \\ &= \mathbf{p}^\top \mathbf{R}^\top \mathbf{R}\mathbf{n}_p + \mathbf{t}^\top \mathbf{R}\mathbf{n}_p \\ &= \mathbf{p}^\top \mathbf{n}_p + (\mathbf{R}^\top \mathbf{t})^\top \mathbf{n}_p, \end{aligned} \quad (6)$$

and we can see that the first term $\mathbf{p}^\top \mathbf{n}_p$ is invariant w.r.t. different poses. To maximize internally visible keypoints in \mathcal{P}_{sym} , we only need to minimize the second term $(\mathbf{R}^\top \mathbf{t})^\top \mathbf{n}_p$ for \mathcal{P}_{sym} .

Base case: single continuous symmetry axis, no additional discrete symmetry. For example, symmetry transformations of a textureless bowl contains continuous rotations around an axis. The symmetry transformations can be parameterized as $\mathbf{R}_*(\theta)$, where $*$ denotes a symmetry axis and θ is the rotation angle around the symmetry axis. For a specific transformation $\mathbf{R}_*(\theta)$, the corresponding transformed rotation is

$$\tilde{\mathbf{R}} = \mathbf{R}\mathbf{R}_*(\theta), \quad (7)$$

and the corresponding transformed translation remains the same, *i.e.*,

$$\tilde{\mathbf{t}} = \mathbf{t}, \quad (8)$$

thus

$$\begin{aligned} (\tilde{\mathbf{R}}^\top \tilde{\mathbf{t}})^\top \mathbf{n}_p &= (\mathbf{R}_*(\theta)^\top \mathbf{R}^\top \mathbf{t})^\top \mathbf{n}_p \\ &= \mathbf{t}^\top \mathbf{R}\mathbf{R}_*(\theta)\mathbf{n}_p \\ &= (\mathbf{R}^\top \mathbf{t})^\top (\mathbf{R}_*(\theta)\mathbf{n}_p). \end{aligned} \quad (9)$$

Without loss of generality, we can assume z -axis is the symmetry axis. Otherwise, we can apply a simple coordinate system transformation to the object to satisfy this assumption. Consider a special case when $\mathbf{n}_p = \mathbf{n}_0 = [1, 0, 0]^\top$, and then

$$\mathbf{R}_z(\theta)\mathbf{n}_0 = \begin{bmatrix} \cos \theta & -\sin \theta & 0 \\ \sin \theta & \cos \theta & 0 \\ 0 & 0 & 1 \end{bmatrix} \begin{bmatrix} 1 \\ 0 \\ 0 \end{bmatrix} = \begin{bmatrix} \cos \theta \\ \sin \theta \\ 0 \end{bmatrix}, \quad (10)$$

and we further get

$$(\tilde{\mathbf{R}}^\top \tilde{\mathbf{t}})^\top \mathbf{n}_0 = a \cos \theta + b \sin \theta, \quad (11)$$

where a, b are the first and second entry of $\mathbf{R}^\top \mathbf{t}$, respectively. By minimizing $(\tilde{\mathbf{R}}^\top \tilde{\mathbf{t}})^\top \mathbf{n}_0$, we minimize the quantity in Eq. (6) for the point \mathbf{p}_0 with $\mathbf{n}_p = \mathbf{n}_0 = [1, 0, 0]^\top$ and its neighborhood, which ensures the internal visibility of \mathbf{p}_0 and its neighborhood (*i.e.*, \mathcal{P}_{sym}).

For simplicity, denote

$$f(\theta) \stackrel{\text{def}}{=} a \cos \theta + b \sin \theta, \quad (12)$$

and now we need to minimize $f(\theta)$. When $a = 0$, it is straightforward to get $\theta = \pi/2 + [b > 0]\pi$, where $[\cdot]$ is Iverson bracket outputting binary values $\{0, 1\}$. When $a \neq 0$, we have

$$f'(\theta) = -a \sin \theta + b \cos \theta, \quad (13)$$

and $\theta = \arctan(b/a)$ is one of the solutions to make $f'(\theta) = 0$. We also need to consider

$$\begin{aligned} f''(\theta) &= -a \cos \theta - b \sin \theta \\ &= -a \cos \theta \left(1 + \frac{b}{a} \tan \theta\right) \\ &= -a \cos \theta \left(1 + \frac{b^2}{a^2}\right), \end{aligned} \quad (14)$$

and let $f''(\theta) \geq 0$, thus $\theta = \arctan(b/a) + [a > 0]\pi$.

In summary, we modify the original annotated rotation matrix by right-multiplying rotation around z -axis $\mathbf{R}_z(\theta)$,

where θ is the rotation angle around z -axis, and is determined by

$$\theta = \begin{cases} \pi/2 + [b > 0]\pi, & \text{if } a = 0 \\ \arctan(b/a) + [a > 0]\pi, & \text{otherwise} \end{cases}, \quad (15)$$

where a, b are the first and second entry of $\mathbf{R}^\top \mathbf{t}$, respectively, $[\cdot]$ is Iverson bracket outputting binary values $\{0, 1\}$.

Variation I: single continuous symmetry axis, additional discrete symmetry. A textureless cylinder is an example of this symmetry type. We can first use the analytic formula Eq. (15) to resolve the ambiguity caused by continuous symmetry, then enumerate the finite equivalent poses of the discrete symmetry.

Variation II: multiple continuous symmetry axes. A textureless sphere is an example of this symmetry type. Without loss of generality, we can assume y -axis is another symmetry axis. After resolving the ambiguity caused by continuous symmetry of z -axis, we apply additional transformation $\mathbf{R}_y(\phi)$, where ϕ is the rotation angle around y -axis. The derivation of ϕ is very similar to θ in $\mathbf{R}_z(\theta)$, hence we omit it for simplicity.

C. Visibility-Aware Importance via Personalized PageRank

In the previous sections we have discussed how to assign binary labels for keypoint visibility. While visible points are clearly more useful than invisible ones for pose estimation, not all visible points are equally important, depending on the distribution of these points and the specific estimation algorithms. Moreover, if an invisible keypoint is close to visible ones, localizing it may not be difficult. To address these issues, we propose to compute real-valued visibility-aware importance by measuring the closeness to visible keypoints w.r.t. a specific measure of the proximity.

In practice, we adopt Personalized PageRank (PPR) as our proximity measure, which is a variation of PageRank [31] based on a random walk model. Specifically, we build a directed k -nearest neighbor (k -NN) graph G from predefined keypoints \mathcal{P} . For each keypoint \mathbf{p} , we create edges from \mathbf{p} to its k -nearest neighbors. We define transition matrix \mathbf{T} as

$$\mathbf{T} = \frac{1}{k} \mathbf{A}^\top, \quad (16)$$

where \mathbf{A} is the adjacency matrix of G . With probability $c \in (0, 1)$, a random walker on G moves along edges following \mathbf{T}^\top . With probability $1 - c$, the random walker restarts at any visible keypoint with uniform probability. c is often called damping factor, and we assign c the widely used value 0.85. We use the stationary probability distribution \mathbf{r} over N keypoints to measure closeness to visible keypoints, where each entry of \mathbf{r} represents the probability that the random walker resides on the corresponding keypoint. We can obtain \mathbf{r} by solving the following equation

$$\mathbf{r} = c\mathbf{T}\mathbf{r} + (1 - c)\mathbf{s}, \quad (17)$$

where \mathbf{s} is the restart vector, and the entry of keypoint \mathbf{p} is determined from binary visibility labels as

$$\mathbf{s}(\mathbf{p}) = \begin{cases} 1/N_{\text{vis}}, & \text{if } V(\mathbf{p}) = 1 \\ 0, & \text{otherwise} \end{cases}, \quad (18)$$

where N_{vis} denotes the number of visible keypoints. By rearranging Eq. (17), we can compute \mathbf{r} as

$$\mathbf{r} = \mathbf{T}_{\text{ppr}}\mathbf{s}, \quad (19)$$

where

$$\mathbf{T}_{\text{ppr}} \stackrel{\text{def}}{=} (1 - c)(\mathbf{I} - c\mathbf{T})^{-1}. \quad (20)$$

Note that \mathbf{T}_{ppr} is well-defined in Eq. (20) because $\mathbf{I} - c\mathbf{T}$ is invertible. Moreover, \mathbf{T}_{ppr} is invariant for the object, so we can precompute \mathbf{T}_{ppr} using Eq. (20) and store it, and then we can obtain our visibility-aware importance \mathbf{r} from any input binary labels using only one matrix-vector multiplication (Eq. (19)).

Besides the efficient computation of importance \mathbf{r} , PPR also utilizes the overall structure of the object via the random walker on G . In contrast, other popular measures may focus on limited structure information, e.g., shortest paths. As a result, PPR is less impacted by outliers in visible keypoints, which makes the computation of \mathbf{r} more robust.

D. From Visibility-Aware Importance to Pose Estimation

To improve 6DoF pose estimation, we propose to localize keypoints with high visibility-aware importance \mathbf{r} (Eq. (19)). One feasible way is to train a network to directly regress \mathbf{r} . However, precisely producing importance of each keypoint is difficult. We instead obtain \mathbf{r} in an alternative way. We first use binary classifiers to predict binary visibility V (Section III-A) and compute restart vector \mathbf{s} (Eq. (18)), then we get importance \mathbf{r} using Eq. (19). In this way, we only need to train binary classifiers, which is typically easier than training regression models. Besides, as discussed in Section III-C, our proposed PPR-based importance is robust against outliers in visibility estimation.

Our proposed visibility-aware importance \mathbf{r} can be easily integrated into existing keypoint-based 6DoF pose estimators. We adopt the recent state-of-the-art open-source method CheckerPose [21] as our base. CheckerPose utilizes GNNs to explicitly model the interactions among dense keypoints, and predicts binary codes as a hierarchical representation of 2D locations. Besides, CheckerPose exploits a CNN decoder to learn image features and fuses the features into the GNN branch. To facilitate mini-batch-based training for GNNs, we select $N' = N/2$ keypoints with highest importance for localization. For extreme case when the ratio of estimated visible keypoints is below a certain threshold, we directly use N' evenly distributed keypoints for robustness.

As shown in Figure 3, we use a backbone network to extract image features from input region of interest (RoI) I_O of object O . Then we utilize a multi-label classifier to predict external visibility $V_{\text{ex}}(\mathbf{p})$ and internal visibility $V_{\text{in}}(\mathbf{p})$ for each keypoint $\mathbf{p} \in \mathcal{P}$. Each decomposed visibility focuses on a specific factor as discussed in Section III-A. Within the classifier, we adopt a shallow GNN on k -NN graph G described in Section III-C, to improve the classification consistency for connected keypoints. After estimating $V_{\text{ex}}(\mathbf{p}), V_{\text{in}}(\mathbf{p})$, we can get overall binary visibility $V(\mathbf{p})$ by simply multiplying $V_{\text{ex}}(\mathbf{p})$ and $V_{\text{in}}(\mathbf{p})$. From the predicted binary visibility of each keypoint, we generate real-valued visibility-aware importance using PPR based algorithm (Eq. (19)). The coefficient matrix

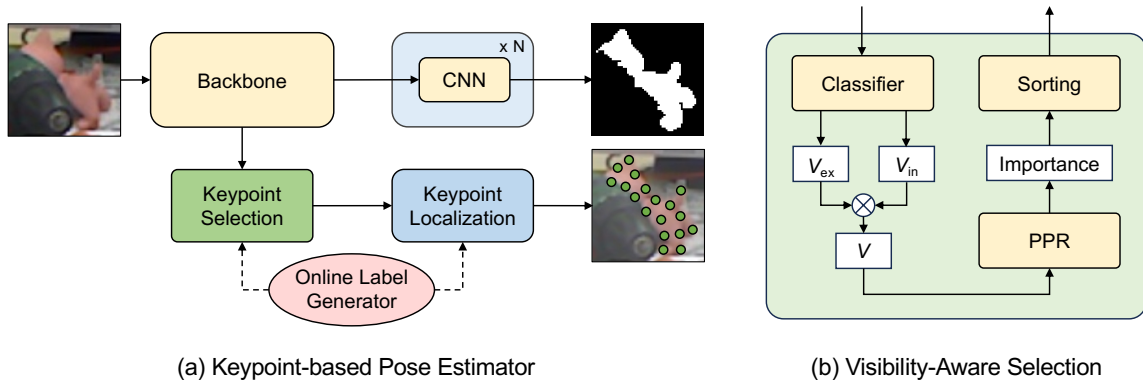


Fig. 3. **Illustration of our visibility-aware pose estimator.** (a) Overall architecture: We use a backbone network to extract image features from the input image, and select keypoints with high visibility-aware importance for localization. We generate supervision signals online for keypoint visibility and localization. We also train object segmentation with available ground truth masks (omitted in the figure). (b) Details of visibility-aware selection module: For each keypoint, we use a multi-label classifier to predict external visibility V_{ex} and internal visibility V_{in} . We then obtain overall visibility V , and adopt Personalized PageRank (PPR) to generate visibility-aware importance from V . We finally sort importance and select keypoints with high importance.

\mathbf{T}_{ppr} is precomputed using Eq. (20), so we only need to create restart vector \mathbf{s} from binary visibility (Eq. (18)) and run a simple matrix-vector multiplication. We then select $N' = N/2$ keypoints with highest importance, denoted as $\mathcal{P}_{vis} \subset \mathcal{P}$. We use the subgraph G_{vis} of G induced by \mathcal{P}_{vis} in GNN-based localization process.

We further enhance keypoint embedding to improve the network performance. Specifically, We use a shallow GNN to obtain 64-dim embedding F_P from the coordinates of \mathcal{P} , and concatenate it with initial keypoint embedding in G . We can regard F_P as positional encoding [9], [70], which facilitates the localization of the dynamic subgraph G_{vis} .

E. Two-stage Training

We train our visibility-aware pose estimator in a supervised manner. As shown in Figure 3, with object-level annotations, we generate binary labels of visibility described in Section III-A on the fly during training. Note that other supervision signals are either directly available (e.g., segmentation masks) or can also be efficiently generated on the fly (e.g., 2D locations of the keypoints).

While the whole network can be trained from scratch, it is often inefficient since the graph G_{vis} may vary significantly for the same input image I when visibility prediction is unstable. We instead use a two-stage training procedure inspired by CheckerPose [21]. At the first stage, we train network layers corresponding to low-level estimations, including external visibility V_{ex} , internal visibility V_{in} , 1-bit indicator code \mathbf{b}_v , and the first d_0 bits of $\mathbf{b}_x, \mathbf{b}_y$ ($\mathbf{b}_v, \mathbf{b}_x$ and \mathbf{b}_y are defined in CheckerPose). We treat the prediction of these low-level quantities as binary classification tasks, and use binary cross-entropy loss for training. At the second stage, we train the whole network. We use binary cross-entropy loss for visibility estimation and binary code generation, and apply L_1 loss for segmentation mask prediction.

F. Extension for CAD-Free Object Pose Estimation

So far we have assumed that the 3D CAD model is available for keypoint sampling and visibility label generation. When the

3D CAD model is unavailable, a straightforward solution is to reconstruct a 3D mesh from a set of posed RGB images. With the advancement of image-based mesh reconstruction techniques, we can make use of an off-the-shelf image-based mesh reconstructor, waiving the cumbersome procedure of designing and training a reconstructor specific to an object in interest. In practice, we adopt Wonder3D [71] which can generate a textured 3D mesh from an single-view input.

The biggest problem of using image-based reconstruction is the imperfect reconstruction quality. We notice that though Wonder3D can generate plausible reconstruction for the visible part in the input view, the reconstructed hidden part may significantly deviate from ground truth. To address this issue, for each object, we use m views to reconstruct m 3D meshes, instead of reconstructing a single 3D mesh. For each reconstructed mesh, we use the criteria in Section III-A to determine the visible vertices in the corresponding input view, from which we uniformly sample N/m keypoints. In this way, we obtain predefined N keypoints with plausible 3D coordinates and normals. Furthermore, when generating synthetic training images, for each randomly sampled pose, we render the mesh that is reconstructed from the closest view.

Once we sample 3D keypoints on the object surface and generate sufficient training images, we can train VAPO following the CAD-based setting.

IV. EXPERIMENTS

A. Experimental Setup

Implementation Details. We implement our method using PyTorch [72]. We train our network using the Adam optimizer [73] with a batch size of 32 and learning rate of $2e-4$. We adopt CheckerPose [21] as our base keypoint localization method, and follow it to use $N = 512$ predefined keypoints and $k = 20$ nearest neighbors for k -NN graph. We select $N' = 256$ keypoints and use the induced subgraph in the localization step. For the binary code generation, we set the number of bits d as 7, and the number of initial bits d_0 as 3. Following the common practice [18], [20], [21], [23], [25],

TABLE I
EVALUATION OF VISIBILITY PREDICTION. WE REPORT AVERAGE ACCURACY, PRECISION, RECALL, AND F1 SCORE OF EXTERNAL VISIBILITY V_{ex} AND INTERNAL VISIBILITY V_{in} ON THREE DATASETS.

Dataset	V_{ex}				V_{in}			
	Acc.	Prec.	Recall	F1	Acc.	Prec.	Recall	F1
LM [32]	92.6	94.2	97.7	95.9	98.1	98.2	97.9	98.0
LM-O [33]	87.4	84.6	85.6	84.6	91.7	91.4	91.7	91.5
YCB-V [34]	91.8	94.2	94.1	94.0	95.8	95.6	95.7	95.6

we use an off-the-shelf object detector to extract region of the object in interest during inference. For the LM dataset, we use Faster-RCNN [74] detector provided by [18]. For the LM-O and YCB-V datasets, we use FCOS [75] detector provided by CDPNv2 [18]. We use Progressive-X [24] to obtain object poses from correspondences for all experiments. We run Progressive-X for 400 iterations with the threshold of reprojection error as 2 pixels. For the CAD-free setting, we use $m = 8$ views for reconstruction.

Datasets. Following the common practice, we conduct extensive experiments on Linemod (LM) [32], Linemod-Occlusion (LM-O) [33], and YCB-V [34]. LM contains 13 objects, and provides around 1,200 real images for each object with mild occlusions. Following [76], we use about 15% images as training set and test our method on the remaining images. We also use 1,000 synthetic training images for each object following [18], [23], [25]. LM-O contains 8 objects from LM, and uses the real images from LM as training images. The test set is composed of 1,214 real images with severe occlusions and clutters. YCB-V contains 21 daily objects and provides more than 110,000 real images with severe occlusions and clutters. For training on LM-O and YCB-V, we follow the recent trend [20], [21], [23] and use the physically-based rendered data [77] as additional training images.

Evaluation Metrics. We adopt the commonly-used metric ADD(-S) to evaluate the estimated poses. To compute ADD(-S) with threshold $x\%$, we transform the 3D model points using the predicted poses and the ground truth, compute the average distance between the transformed results, and check whether the average distance is below $x\%$ of the object diameter. For symmetric objects, we compute the average distance based on the closest points. On YCB-V, we follow the common practice [20], [23], [43] to report the AUC (area under curve) of ADD-S and ADD(-S) [34], where the symmetric metric is used for all objects in ADD-S but for symmetric objects only in ADD(-S). The AUC metric reflects the accumulated performance across different thresholds, and provides complementary evaluation to ADD(-S). For keypoint-based methods, we compute average localization error by comparing the predicted keypoint locations and ground truth. We also report the inlier ratio with threshold of x pixels.

B. Visibility Prediction

We first demonstrate that visibility classification is a relatively easy task to enable reliable keypoint selection for

TABLE II
EVALUATION OF KEYPOINT LOCALIZATION. WE COMPARE OUR METHOD WITH CHECKERPOSE [21]. WE REPORT THE AVERAGE LOCALIZATION ERROR, AND INLIER RATIO WITH TWO THRESHOLDS (2 PIXELS AND 5 PIXELS).

Dataset	LM [32]		LM-O [33]		YCB-V [34]	
	[21]	Ours	[21]	Ours	[21]	Ours
Error (pixel)	3.4	3.1	14.4	14.4	10.9	8.7
Inlier-2px (%)	44.8	67.4	19.4	24.3	8.4	15.2
Inlier-5px (%)	88.4	88.4	67.8	71.7	39.6	55.2

TABLE III
ABLATION STUDY ON THE LM DATASET.

Method	ADD(-S)			MEAN
	0.02d	0.05d	0.1d	
GDR-Net [23]	35.5	76.3	93.7	68.5
SO-Pose [25]	45.9	83.1	96.0	75.0
EPro-PnP [78]	44.8	82.0	95.8	74.2
CheckerPose [21]	35.7	84.5	97.1	72.4
Ours (w/o Selection, $N = 256$)	44.7	84.3	96.9	75.3
Ours (w/o Selection, $N = 512$)	45.5	84.0	96.4	75.3
Ours (w/o V_{ex})	48.1	85.6	96.9	76.9
Ours (w/o V_{in})	36.0	76.0	93.9	68.6
Ours (w/o P. E.)	46.6	84.4	96.6	75.9
Ours (w/o Two-stage)	45.4	83.9	96.1	75.1
Ours ($N' = 128$)	37.6	79.4	95.6	70.9
Ours ($N' = 192$)	45.4	84.6	96.8	75.6
Ours ($N' = 320$)	48.6	85.8	97.0	77.1
Ours ($N' = 256$)	48.6	85.9	97.0	77.2

localization. For the prediction of external visibility V_{ex} and internal visibility V_{in} , we compute accuracy, precision, recall, and F1 score. All metrics are evaluated on the networks after 50k training steps in the first stage. We report average results on the three datasets in Table I. As shown in Table I, a simple classifier is capable of producing good estimations.

C. Keypoint Localization

We evaluate keypoint localization in Table II and compare with our baseline method CheckerPose [21]. For the LM dataset where the occlusions are mild, we significantly increase the inlier ratio with the stricter threshold (2 pixels) and achieve comparable performance with threshold of 5 pixels. For the LM-O and YCB-V datasets with severe occlusions and clutters, we significantly boost the inlier ratio. The results clearly show that our visibility-aware strategy improves the quality of 3D-2D correspondences.

D. Ablation Study on LM Dataset

We report ablation studies on LM [32] in Table III. We train a unified pose estimator for all 13 objects. We first train the layers generating low-level quantities for 50k steps with learning rate of $2e-4$, then we train all network layers for 100k steps, and finally reduce the learning rate to $1e-4$ and train 20k steps.

TABLE IV

COMPARISON ON LM-O. WE REPORT THE AVERAGE RECALL (%) OF ADD(-S) WITH THREE THRESHOLDS: 0.02D, 0.05D, AND 0.1D. WE HIGHLIGHT THE BEST RESULT AND THE SECOND BEST RESULT IN RED AND BLUE, RESPECTIVELY.

Method	GDR [23]	Zebra [20]	LC [43]	Checker [21]	Ours
0.02d	4.4	9.8	8.6	7.3	9.7
0.05d	31.1	44.6	44.2	43.5	46.2
0.1d	62.2	76.9	78.06	77.5	78.02
Mean	32.6	43.8	43.6	42.8	44.6

Effectiveness of Visibility-Aware Keypoint Selection. We report the performance of using a fixed set of N evenly distributed keypoints in localization step in Table III. The results (denoted as w/o Selection) with $N = 256$ and $N = 512$ degrade especially for ADD(-S) 0.02d, which clearly demonstrates the effectiveness of our visibility-aware keypoint selection scheme.

Effectiveness of Dual Visibility Estimation. Our methods select keypoints based on both external visibility V_{ex} and internal visibility V_{in} . Since the external occlusion is mild in test data of LM dataset, self-occlusion is the major factor of invisibility. As shown in Table III, selecting keypoints based on V_{in} (denoted as w/o V_{ex}) can significantly boost the performance compared with w/o Selection. Incorporating V_{ex} further improves the performance.

Effectiveness of Positional Encoding. In Table III, we also present the result without positional encoding (denoted as w/o P. E.). Since the selected keypoints are dynamic w.r.t. input images, we find that adding positional encoding greatly improves the performance.

Effectiveness of Two-stage Training. In Table III, we also report the performance without two-stage training (denoted as w/o Two-stage). The overall performance degrades without two-stage training, since the induced subgraph G_{vis} is not stable when the visibility estimator does not converge.

Number of Selected Keypoints. We show the results with different number of selected keypoints (N') in Table III. The performance improves when N' is gradually increased towards 256, and remains almost the same when N' is increased to 320 with more computational cost. We use $N' = 256$ in practice.

E. Comparison to State of the Art

Experiments on LM. As shown in Table III, our method significantly improves the performance w.r.t. ADD(-S) with threshold 2% and 5% (denoted as 0.02d and 0.05d). This demonstrates that our visibility-aware framework can greatly increase the ratio of qualified poses w.r.t. a strict threshold. Our method achieves comparable results w.r.t. ADD(-S) with threshold 10% (denoted as 0.1d). The average of the metrics is the best among all methods.

Experiments on LM-O. Following [20], [21], [23], [43], we train a single pose estimator for each object on LM-O dataset. For the two-stage training procedure, we set the first stage as 50k steps and the second stage as 700k steps. We report the average recall of ADD(-S) metric with three

TABLE V

COMPARISON ON YCB-V. WE REPORT THE AVERAGE ADD(-S), AND AUC OF ADD-S AND ADD(-S). AUC VALUES COMPUTED WITHOUT AND WITH 11-POINT INTERPOLATION ARE DENOTED AS “w/o” AND “w/ IT”, RESPECTIVELY. “-” DENOTES UNAVAILABLE RESULTS.

Method	ADD(-S)	AUC-S		AUC(-S)	
		w/o	w/ IT	w/o	w/ IT
SegDriven [14]	39.0	-	-	-	-
S. Stage [44]	53.9	-	-	-	-
RePose [79]	62.1	88.5	-	82.0	-
GDR-Net [23]	60.1	-	91.6	-	84.4
SO-Pose [25]	56.8	-	90.9	-	83.9
Zebra [20]	80.5	90.1	-	85.3	-
DProST [80]	65.1	-	-	77.4	-
Checker [21]	81.4	91.3	95.3	86.4	91.1
Zebra-LC [43]	82.4	90.8	95.0	86.1	90.8
Ours	84.9	92.3	96.4	87.9	92.7

TABLE VI

CAD-FREE OBJECT POSE ESTIMATION ON LM DATASET. WE REPORT THE AVERAGE RECALL (%) OF ADD(-S) WITH THRESHOLD OF 0.1D.

Method	RLLG [46]	One [47]	One++ [48]	GS [49]	Ours
ape	52.9	11.8	31.2	71.0	83.4
benchv.	96.5	92.6	97.3	99.8	98.9
camera	87.8	88.1	88.0	98.2	95.9
can	86.8	77.2	89.8	97.7	99.4
cat	67.3	47.9	70.4	86.7	94.7
driller	88.7	74.5	92.5	96.2	96.7
duck	54.7	34.2	42.3	77.2	82.4
eggbox	94.7	71.3	99.7	99.6	99.6
glue	91.9	37.5	48.0	98.4	99.4
holep.	75.4	54.9	69.7	87.4	90.9
iron	94.5	89.2	97.4	99.2	95.3
lamp	96.6	87.6	97.8	98.9	99.1
phone	89.2	60.6	76.0	85.0	93.7
mean	82.9	63.6	76.9	92.0	94.6

thresholds (0.02d, 0.05d, and 0.1d) in Table IV. As shown in Table IV, our visibility-aware keypoint localization scheme clearly boosts our base CheckerPose [21] on all three thresholds. Our method also greatly surpasses previous methods w.r.t. 0.05d threshold and the mean of three thresholds, and achieves comparable performance w.r.t. other thresholds.

Experiments on YCB-V. Following [20], [21], [23], [43], we train a single pose estimator for each object on YCB-V dataset. For the two-stage training procedure, we set the first stage as 50k steps and the second stage as 250k steps. We report the average values of ADD(-S) (0.1d) and AUC metrics in Table V. Our method significantly improves the pose estimation performance w.r.t. the ADD(-S). Our method also achieves the best performance w.r.t. metrics based on AUC, which indicates that our method achieves the best accumulated performance across various thresholds.

F. CAD-Free Object Pose Estimation on LM Dataset

In addition to the classical CAD-based setting, we also evaluate our method in the CAD-free setting on the LM dataset. We train a unified pose estimator for all 13 objects. After training the layers generating low-level quantities for 50k

TABLE VII
RUNTIME ANALYSIS.

Method	Corr.	PnP	Overall
Zebra [20]	13.6	304.2	317.8
Checker [21]	68.4	33.4	101.8
Ours	68.3	31.3	99.6

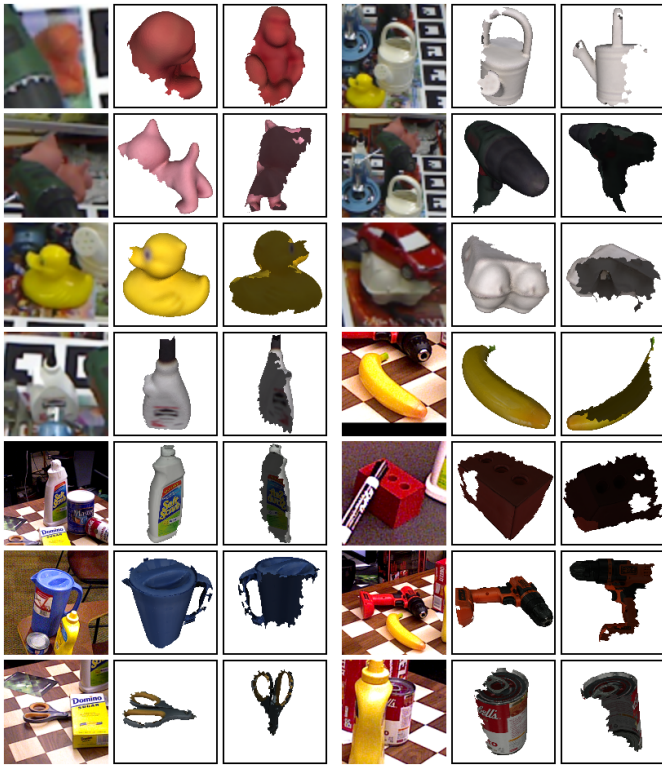


Fig. 4. **Visualization of selected keypoints.** For better visualization, we interpolate the corresponding 3D meshes of the selected keypoints with textures. Note due to the interpolation, the boundary of the meshes may look noisy. For each input image of an object in interest, we present the mesh with two different views for comprehensive visualization.

steps with learning rate of $2e-4$, we train all network layers for 200k steps and then reduce the learning rate to $1e-4$ and train 200k steps. As shown in Table VI, our method significantly outperforms recent CAD-free baselines in terms of the ADD(-S) (0.1d) metric, which demonstrates the capability of our method to handle the more challenging CAD-free setting.

G. Runtime Analysis

In Table VII, we report the running speed of the methods that first establish dense correspondences and then use Progressive-X [24] as PnP solver. For an input 640×480 RGB image, we evaluate the speed on a desktop with an Intel 2.30GHz CPU and an NVIDIA TITAN RTX GPU. The results show clear speed advantage of our method in addition to achieving state-of-the-art accuracies.

H. Visualization

Visualization of Selected Keypoints. In Figure 4, we provide qualitative results of our visibility-aware keypoint

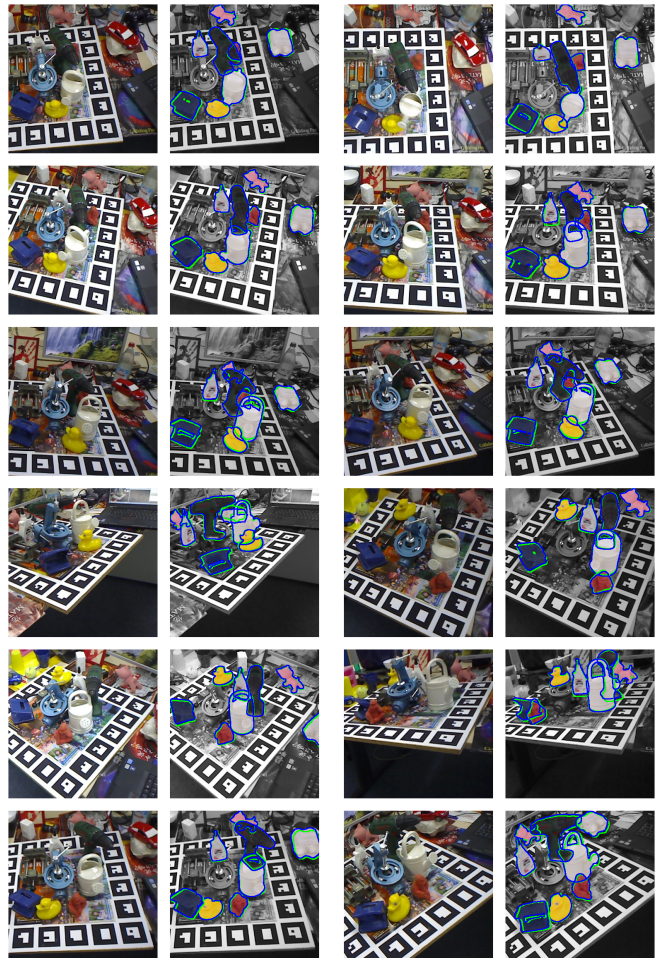


Fig. 5. **Qualitative results on the LM-O dataset.** For input image on the left, we visualize 6D pose on the right by rendering the 3D CAD models. Green contour denotes ground truth and blue contour denotes the prediction from our method.

selection. Since it is hard to see the correspondences between an input image and a point cloud of selected keypoints, we compute the selection results of all vertices of the CAD models by nearest neighbor interpolation over the selection of 512 keypoints. We then visualize the faces whose vertices are all selected. We present results of various objects with different external occlusion and self-occlusion, demonstrating that our proposed visibility-aware keypoint selection module is capable of selecting reasonable keypoints for reliable 3D-2D correspondences.

Qualitative Results. We present qualitative results of our methods for LM-O [33] and YCB-V [34] in Figure 5 and Figure 6, respectively. The qualitative results demonstrate that our method can generate accurate and robust estimations for severely occluded objects.

V. CONCLUSION

We propose a novel visibility-aware keypoint-based method, named VAPO, for instance-level 6DoF object pose estimation with and without 3D CAD models. By localizing the important keypoints guided by visibility, we efficiently invest compu-



Fig. 6. **Qualitative results on the YCB-V dataset.** For each input image on the left, we visualize 6DoF pose on the right by rendering the 3D CAD models. Green contour denotes ground truth and blue contour denotes the prediction from our method.

tational resources to establish more reliable 3D-2D correspondences. From object-level annotations, we generate binary keypoint visibility labels as well as real-valued visibility-aware importance, for both asymmetric and symmetric objects. The extensive experiments on LM, LM-O and YCB-V datasets demonstrate that our method significantly improves both keypoint localization and object pose estimation.

REFERENCES

[1] M. Zhu, K. G. Derpanis, Y. Yang, S. Brahmabhatt, M. Zhang, C. Phillips, M. Lecce, and K. Daniilidis, "Single image 3d object detection and pose estimation for grasping," in *2014 IEEE International Conference on Robotics and Automation (ICRA)*. IEEE, 2014, pp. 3936–3943.

[2] J. Tremblay, T. To, B. Sundaralingam, Y. Xiang, D. Fox, and S. Birchfield, "Deep object pose estimation for semantic robotic grasping of household objects," in *Conference on Robot Learning*. PMLR, 2018, pp. 306–316.

[3] J. Tremblay, S. Tyree, T. Mosier, and S. Birchfield, "Indirect object-to-robot pose estimation from an external monocular rgb camera," in *2020 IEEE/RSJ International Conference on Intelligent Robots and Systems (IROS)*. IEEE, 2020, pp. 4227–4234.

[4] F. Manhardt, W. Kehl, and A. Gaidon, "ROI-10D: monocular lifting of 2d detection to 6d pose and metric shape," in *Proceedings of the IEEE/CVF Conference on Computer Vision and Pattern Recognition (CVPR)*, 2019, pp. 2069–2078.

[5] D. Wu, Z. Zhuang, C. Xiang, W. Zou, and X. Li, "6D-VNet: end-to-end 6-dof vehicle pose estimation from monocular RGB images," in *Proceedings of the IEEE/CVF Conference on Computer Vision and Pattern Recognition Workshops*, 2019, pp. 0–0.

[6] S. Li, Z. Yan, H. Li, and K.-T. Cheng, "Exploring intermediate representation for monocular vehicle pose estimation," in *Proceedings of the IEEE/CVF Conference on Computer Vision and Pattern Recognition (CVPR)*, 2021, pp. 1873–1883.

[7] E. Marchand, H. Uchiyama, and F. Spindler, "Pose estimation for augmented reality: a hands-on survey," *IEEE transactions on visualization and computer graphics*, vol. 22, no. 12, pp. 2633–2651, 2015.

[8] F. Tang, Y. Wu, X. Hou, and H. Ling, "3d mapping and 6d pose computation for real time augmented reality on cylindrical objects," *IEEE Transactions on Circuits and Systems for Video Technology*, vol. 30, no. 9, pp. 2887–2899, 2019.

[9] B. Mildenhall, P. P. Srinivasan, M. Tancik, J. T. Barron, R. Ramamoorthi, and R. Ng, "Nerf: Representing scenes as neural radiance fields for view synthesis," in *Proceedings of the European Conference on Computer Vision (ECCV)*, 2020.

[10] Z. Wang, S. Wu, W. Xie, M. Chen, and V. A. Prisacariu, "Nerf: Neural radiance fields without known camera parameters," *arXiv preprint arXiv:2102.07064*, 2021.

[11] M. Rad and V. Lepetit, "BB8: a scalable, accurate, robust to partial occlusion method for predicting the 3d poses of challenging objects without using depth," in *Proceedings of the IEEE International Conference on Computer Vision (ICCV)*, 2017, pp. 3828–3836.

[12] B. Tekin, S. N. Sinha, and P. Fua, "Real-time seamless single shot 6d object pose prediction," in *Proceedings of the IEEE Conference on Computer Vision and Pattern Recognition (CVPR)*, 2018, pp. 292–301.

[13] M. Oberweger, M. Rad, and V. Lepetit, "Making deep heatmaps robust to partial occlusions for 3d object pose estimation," in *Proceedings of the European Conference on Computer Vision (ECCV)*, 2018, pp. 119–134.

[14] Y. Hu, J. Hugonot, P. Fua, and M. Salzmann, "Segmentation-driven 6d object pose estimation," in *Proceedings of the IEEE/CVF Conference on Computer Vision and Pattern Recognition (CVPR)*, 2019, pp. 3385–3394.

[15] S. Peng, Y. Liu, Q. Huang, X. Zhou, and H. Bao, "PVNet: pixel-wise voting network for 6dof pose estimation," in *Proceedings of the IEEE/CVF Conference on Computer Vision and Pattern Recognition (CVPR)*, 2019, pp. 4561–4570.

[16] S. Zakharov, I. Shugurov, and S. Ilic, "DPOD: 6d pose object detector and refiner," in *Proceedings of the IEEE/CVF International Conference on Computer Vision (ICCV)*, 2019, pp. 1941–1950.

[17] K. Park, T. Patten, and M. Vincze, "Pix2Pose: pixel-wise coordinate regression of objects for 6d pose estimation," in *Proceedings of the IEEE/CVF International Conference on Computer Vision (ICCV)*, 2019, pp. 7668–7677.

[18] Z. Li, G. Wang, and X. Ji, "CDPN: coordinates-based disentangled pose network for real-time rgb-based 6-dof object pose estimation," in *Proceedings of the IEEE/CVF International Conference on Computer Vision (ICCV)*, 2019, pp. 7678–7687.

[19] C. Song, J. Song, and Q. Huang, "HybridPose: 6d object pose estimation under hybrid representations," in *Proceedings of the IEEE/CVF Conference on Computer Vision and Pattern Recognition (CVPR)*, 2020, pp. 431–440.

[20] Y. Su, M. Saleh, T. Fetzter, J. Rambach, N. Navab, B. Busam, D. Stricker, and F. Tombari, "ZebraPose: coarse to fine surface encoding for 6dof object pose estimation," in *Proceedings of the IEEE/CVF Conference on Computer Vision and Pattern Recognition (CVPR)*, 2022, pp. 6738–6748.

[21] R. Lian and H. Ling, "Checkerpose: Progressive dense keypoint localization for object pose estimation with graph neural network," in *Proceedings of the IEEE/CVF International Conference on Computer Vision (ICCV)*, October 2023, pp. 14 022–14 033.

[22] V. Lepetit, F. Moreno-Noguer, and P. Fua, "Epnnp: An accurate o (n) solution to the pnp problem," *International journal of computer vision*, vol. 81, no. 2, p. 155, 2009.

[23] G. Wang, F. Manhardt, F. Tombari, and X. Ji, "GDR-Net: geometry-guided direct regression network for monocular 6d object pose estimation," in *Proceedings of the IEEE/CVF Conference on Computer Vision and Pattern Recognition (CVPR)*, 2021, pp. 16 611–16 621.

[24] D. Barath and J. Matas, "Progressive-x: Efficient, anytime, multi-model fitting algorithm," in *Proceedings of the IEEE/CVF International Conference on Computer Vision (ICCV)*, 2019, pp. 3780–3788.

[25] Y. Di, F. Manhardt, G. Wang, X. Ji, N. Navab, and F. Tombari, "SO-Pose: exploiting self-occlusion for direct 6d pose estimation," in *Proceedings of the IEEE/CVF International Conference on Computer Vision (ICCV)*, 2021, pp. 12 396–12 405.

[26] Z. Zhao, G. Peng, H. Wang, H.-S. Fang, C. Li, and C. Lu, "Estimating 6d pose from localizing designated surface keypoints," *arXiv preprint arXiv:1812.01387*, 2018.

[27] S. Johnson and M. Everingham, "Clustered pose and nonlinear appearance models for human pose estimation," in *bmvc*, vol. 2, no. 4. Aberystwyth, UK, 2010, p. 5.

- [28] M. Andriluka, L. Pishchulin, P. Gehler, and B. Schiele, “2d human pose estimation: New benchmark and state of the art analysis,” in *Proceedings of the IEEE Conference on Computer Vision and Pattern Recognition*, 2014, pp. 3686–3693.
- [29] S. Kumar, D. Manocha, B. Garrett, and M. Lin, “Hierarchical back-face culling,” in *7th Eurographics Workshop on Rendering*. Citeseer, 1996, pp. 231–240.
- [30] H. Zhang and K. E. Hoff III, “Fast backface culling using normal masks,” in *Proceedings of the 1997 symposium on Interactive 3D graphics*, 1997, pp. 103–ff.
- [31] L. Page, S. Brin, R. Motwani, and T. Winograd, “The pagerank citation ranking: Bring order to the web,” Technical report, stanford University, Tech. Rep., 1998.
- [32] S. Hinterstoisser, V. Lepetit, S. Ilic, S. Holzer, G. Bradski, K. Konolige, and N. Navab, “Model based training, detection and pose estimation of texture-less 3d objects in heavily cluttered scenes,” in *Asian Conference on Computer Vision (ACCV)*. Springer, 2012, pp. 548–562.
- [33] E. Brachmann, A. Krull, F. Michel, S. Gumhold, J. Shotton, and C. Rother, “Learning 6d object pose estimation using 3d object coordinates,” in *Proceedings of the European Conference on Computer Vision (ECCV)*. Springer, 2014, pp. 536–551.
- [34] Y. Xiang, T. Schmidt, V. Narayanan, and D. Fox, “PoseCNN: a convolutional neural network for 6d object pose estimation in cluttered scenes,” in *Robotics: Science and Systems*, 2018.
- [35] D. P. Huttenlocher, G. A. Klanderman, and W. J. Rucklidge, “Comparing images using the hausdorff distance,” *IEEE Transactions on pattern analysis and machine intelligence*, vol. 15, no. 9, pp. 850–863, 1993.
- [36] C. Gu and X. Ren, “Discriminative mixture-of-templates for viewpoint classification,” in *Proceedings of European Conference on Computer Vision (ECCV)*. Springer, 2010, pp. 408–421.
- [37] S. Hinterstoisser, C. Cagniart, S. Ilic, P. Sturm, N. Navab, P. Fua, and V. Lepetit, “Gradient response maps for real-time detection of textureless objects,” *IEEE transactions on pattern analysis and machine intelligence*, vol. 34, no. 5, pp. 876–888, 2011.
- [38] S. Tulsiani and J. Malik, “Viewpoints and keypoints,” in *Proceedings of the IEEE Conference on Computer Vision and Pattern Recognition (CVPR)*, 2015, pp. 1510–1519.
- [39] H. Su, C. R. Qi, Y. Li, and L. J. Guibas, “Render for CNN: viewpoint estimation in images using cnns trained with rendered 3d model views,” in *Proceedings of the IEEE International Conference on Computer Vision (ICCV)*, 2015, pp. 2686–2694.
- [40] W. Kehl, F. Manhardt, F. Tombari, S. Ilic, and N. Navab, “SSD-6D: making rgb-based 3d detection and 6d pose estimation great again,” in *Proceedings of the IEEE International Conference on Computer Vision (ICCV)*, 2017, pp. 1521–1529.
- [41] M. Sundermeyer, Z.-C. Marton, M. Durner, M. Brucker, and R. Triebel, “Implicit 3d orientation learning for 6d object detection from rgb images,” in *Proceedings of the European Conference on Computer Vision (ECCV)*, 2018, pp. 699–715.
- [42] G. Pitteri, A. Bugeau, S. Ilic, and V. Lepetit, “3d object detection and pose estimation of unseen objects in color images with local surface embeddings,” in *Proceedings of the Asian Conference on Computer Vision*, 2020.
- [43] F. Liu, Y. Hu, and M. Salzmann, “Linear-covariance loss for end-to-end learning of 6d pose estimation,” in *Proceedings of the IEEE/CVF International Conference on Computer Vision (ICCV)*, October 2023, pp. 14 107–14 117.
- [44] Y. Hu, P. Fua, W. Wang, and M. Salzmann, “Single-stage 6d object pose estimation,” in *Proceedings of the IEEE/CVF Conference on Computer Vision and Pattern Recognition (CVPR)*, 2020, pp. 2930–2939.
- [45] Y. Hu, S. Speierer, W. Jakob, P. Fua, and M. Salzmann, “Wide-depth-range 6d object pose estimation in space,” in *Proceedings of the IEEE/CVF Conference on Computer Vision and Pattern Recognition (CVPR)*, 2021, pp. 15 870–15 879.
- [46] M. Cai and I. Reid, “Reconstruct locally, localize globally: A model free method for object pose estimation,” in *Proceedings of the IEEE/CVF Conference on Computer Vision and Pattern Recognition*, 2020, pp. 3153–3163.
- [47] J. Sun, Z. Wang, S. Zhang, X. He, H. Zhao, G. Zhang, and X. Zhou, “Onepose: One-shot object pose estimation without cad models,” in *Proceedings of the IEEE/CVF Conference on Computer Vision and Pattern Recognition*, 2022, pp. 6825–6834.
- [48] X. He, J. Sun, Y. Wang, D. Huang, H. Bao, and X. Zhou, “Onepose++: Keypoint-free one-shot object pose estimation without cad models,” *Advances in Neural Information Processing Systems*, vol. 35, pp. 35 103–35 115, 2022.
- [49] D. Cai, J. Heikkilä, and E. Rahtu, “Gs-pose: Cascaded framework for generalizable segmentation-based 6d object pose estimation,” *arXiv preprint arXiv:2403.10683*, 2024.
- [50] B. Kerbl, G. Kopanas, T. Leimkühler, and G. Drettakis, “3d gaussian splatting for real-time radiance field rendering,” *ACM Trans. Graph.*, vol. 42, no. 4, pp. 139–1, 2023.
- [51] W. Hutchcroft, Y. Li, I. Boyadzhiiev, Z. Wan, H. Wang, and S. B. Kang, “Covispose: Co-visibility pose transformer for wide-baseline relative pose estimation in 360° indoor panoramas,” in *European Conference on Computer Vision*. Springer, 2022, pp. 615–633.
- [52] H. Rhodin, N. Robertini, C. Richardt, H.-P. Seidel, and C. Theobalt, “A versatile scene model with differentiable visibility applied to generative pose estimation,” in *Proceedings of the IEEE International Conference on Computer Vision*, 2015, pp. 765–773.
- [53] B. Lee and D. D. Lee, “Online learning of visibility and appearance for object pose estimation,” in *2016 IEEE/RSSJ International Conference on Intelligent Robots and Systems (IROS)*. IEEE, 2016, pp. 2792–2798.
- [54] A. Newell, K. Yang, and J. Deng, “Stacked hourglass networks for human pose estimation,” in *Computer Vision–ECCV 2016: 14th European Conference, Amsterdam, The Netherlands, October 11–14, 2016, Proceedings, Part VIII 14*. Springer, 2016, pp. 483–499.
- [55] P. Hu and D. Ramanan, “Bottom-up and top-down reasoning with hierarchical rectified gaussians,” in *Proceedings of the IEEE Conference on Computer Vision and Pattern Recognition*, 2016, pp. 5600–5609.
- [56] Z. Geng, K. Sun, B. Xiao, Z. Zhang, and J. Wang, “Bottom-up human pose estimation via disentangled keypoint regression,” in *Proceedings of the IEEE/CVF conference on computer vision and pattern recognition*, 2021, pp. 14 676–14 686.
- [57] T.-Y. Lin, M. Maire, S. Belongie, J. Hays, P. Perona, D. Ramanan, P. Dollár, and C. L. Zitnick, “Microsoft coco: Common objects in context,” in *Computer Vision–ECCV 2014: 13th European Conference, Zurich, Switzerland, September 6–12, 2014, Proceedings, Part V 13*. Springer, 2014, pp. 740–755.
- [58] N. D. Reddy, M. Vo, and S. G. Narasimhan, “Occlusion-net: 2d/3d occluded keypoint localization using graph networks,” in *Proceedings of the IEEE/CVF Conference on Computer Vision and Pattern Recognition*, 2019, pp. 7326–7335.
- [59] L. Zhou, Y. Chen, Y. Gao, J. Wang, and H. Lu, “Occlusion-aware siamese network for human pose estimation,” in *Computer Vision–ECCV 2020: 16th European Conference, Glasgow, UK, August 23–28, 2020, Proceedings, Part XX 16*. Springer, 2020, pp. 396–412.
- [60] E. Zhang and G. Turk, “Visibility-guided simplification,” in *IEEE Visualization, 2002. VIS 2002*. IEEE, 2002, pp. 267–274.
- [61] S. Katz, A. Tal, and R. Basri, “Direct visibility of point sets,” *ACM Transactions On Graphics (TOG)*, vol. 26, no. 3, p. 24, 2007.
- [62] S. Katz and A. Tal, “On the visibility of point clouds,” in *Proceedings of the IEEE international conference on computer vision (ICCV)*, 2015, pp. 1350–1358.
- [63] Y. Shi, H. Li, and X. Yu, “Self-supervised visibility learning for novel view synthesis,” in *Proceedings of the IEEE/CVF Conference on Computer Vision and Pattern Recognition (CVPR)*, 2021, pp. 9675–9684.
- [64] P. P. Srinivasan, B. Deng, X. Zhang, M. Tancik, B. Mildenhall, and J. T. Barron, “NeRV: Neural reflectance and visibility fields for relighting and view synthesis,” in *Proceedings of the IEEE/CVF Conference on Computer Vision and Pattern Recognition (CVPR)*, 2021, pp. 7495–7504.
- [65] M. Tancik, V. Casser, X. Yan, S. Pradhan, B. Mildenhall, P. P. Srinivasan, J. T. Barron, and H. Kretzschmar, “Block-NeRF: Scalable large scene neural view synthesis,” in *Proceedings of the IEEE/CVF Conference on Computer Vision and Pattern Recognition (CVPR)*, 2022, pp. 8248–8258.
- [66] Y. Liu, S. Peng, L. Liu, Q. Wang, P. Wang, C. Theobalt, X. Zhou, and W. Wang, “Neural rays for occlusion-aware image-based rendering,” in *Proceedings of the IEEE/CVF Conference on Computer Vision and Pattern Recognition (CVPR)*, 2022, pp. 7824–7833.
- [67] R. Jain, K. K. Singh, M. Hemani, J. Lu, M. Sarkar, D. Ceylan, and B. Krishnamurthy, “Vgflow: Visibility guided flow network for human reposing,” in *Proceedings of the IEEE/CVF Conference on Computer Vision and Pattern Recognition (CVPR)*, 2023, pp. 21 088–21 097.
- [68] R. Zheng, P. Li, H. Wang, and T. Yu, “Learning visibility field for detailed 3d human reconstruction and relighting,” in *Proceedings of the IEEE/CVF Conference on Computer Vision and Pattern Recognition (CVPR)*, 2023, pp. 216–226.
- [69] R. Chen, S. Han, J. Xu, and H. Su, “Visibility-aware point-based multi-view stereo network,” *IEEE transactions on pattern analysis and machine intelligence*, vol. 43, no. 10, pp. 3695–3708, 2020.

- [70] M. Tancik, P. P. Srinivasan, B. Mildenhall, S. Fridovich-Keil, N. Raghavan, U. Singhal, R. Ramamoorthi, J. T. Barron, and R. Ng, "Fourier features let networks learn high frequency functions in low dimensional domains," *Advances in Neural Information Processing Systems*, 2020.
- [71] X. Long, Y.-C. Guo, C. Lin, Y. Liu, Z. Dou, L. Liu, Y. Ma, S.-H. Zhang, M. Habermann, C. Theobalt *et al.*, "Wonder3d: Single image to 3d using cross-domain diffusion," in *Proceedings of the IEEE/CVF Conference on Computer Vision and Pattern Recognition*, 2024, pp. 9970–9980.
- [72] A. Paszke, S. Gross, F. Massa, A. Lerer, J. Bradbury, G. Chanan, T. Killeen, Z. Lin, N. Gimeshain, L. Antiga *et al.*, "Pytorch: An imperative style, high-performance deep learning library," *Advances in neural information processing systems*, vol. 32, pp. 8026–8037, 2019.
- [73] D. P. Kingma and J. Ba, "Adam: A method for stochastic optimization," in *International Conference on Learning Representations (ICLR)*, 2015.
- [74] S. Ren, K. He, R. Girshick, and J. Sun, "Faster R-CNN: towards real-time object detection with region proposal networks," *Advances in neural information processing systems*, vol. 28, pp. 91–99, 2015.
- [75] Z. Tian, C. Shen, H. Chen, and T. He, "FCOS: fully convolutional one-stage object detection," in *Proceedings of the IEEE/CVF International Conference on Computer Vision (ICCV)*, 2019, pp. 9627–9636.
- [76] E. Brachmann, F. Michel, A. Krull, M. Y. Yang, S. Gumhold *et al.*, "Uncertainty-driven 6d pose estimation of objects and scenes from a single rgb image," in *Proceedings of the IEEE Conference on Computer Vision and Pattern Recognition (CVPR)*, 2016, pp. 3364–3372.
- [77] T. Hodaň, M. Sundermeyer, B. Drost, Y. Labbé, E. Brachmann, F. Michel, C. Rother, and J. Matas, "BOP challenge 2020 on 6D object localization," *European Conference on Computer Vision Workshops (ECCVW)*, 2020.
- [78] H. Chen, P. Wang, F. Wang, W. Tian, L. Xiong, and H. Li, "EPro-PnP: generalized end-to-end probabilistic perspective-n-points for monocular object pose estimation," in *Proceedings of the IEEE/CVF Conference on Computer Vision and Pattern Recognition (CVPR)*, 2022, pp. 2781–2790.
- [79] S. Iwase, X. Liu, R. Khirodkar, R. Yokota, and K. M. Kitani, "RePOSE: fast 6d object pose refinement via deep texture rendering," in *Proceedings of the IEEE/CVF International Conference on Computer Vision (ICCV)*, 2021, pp. 3303–3312.
- [80] J. Park and N. I. Cho, "DProST: 6-dof object pose estimation using space carving and dynamic projective spatial transformer," in *Proceedings of the European Conference on Computer Vision (ECCV)*, 2022.